Supplementary Information (SI) for Materials Horizons.

Supplementary information

Ideal Energy-Absorbing Metamaterials Based on Self-locking Bistable Structures

Kuan Liang [1], Xiaopeng Zhang [1,*], Qi Zhao [1], Liujia Suo [2], Zishen Wei [1], Yaguang Wang [1], Yangjun Luo [3], Akihiro Takezawa [4], Dazhi Wang [2]

[1]State Key Laboratory of Structural Analysis, Optimization and CAE Software for Industrial Equipment, Dalian University of Technology, Dalian, 116024, China

[2]Laboratory for Micro/Nano Technology and System of Liaoning Province, Dalian University of Technology, Dalian, 116024, China

[3]School of Science, Harbin Institute of Technology, Shenzhen, 518055, China

[4]Department of Applied Mechanics and Aerospace Engineering, Graduate School of Fundamental Science and Engineering, Waseda University, Tokyo, 169-8555, Japan

*Email: zhangxiaopeng@dlut.edu.cn

S1: Theoretical model for snap-fit structure

To predict the stiffness of the snap-fit structure during the compression process, it was simplified and analyzed theoretically. Figure S1a shows the geometric parameters of the structure. Based on the symmetry of the snap-fit structure, the theoretical analysis was conducted on one side.

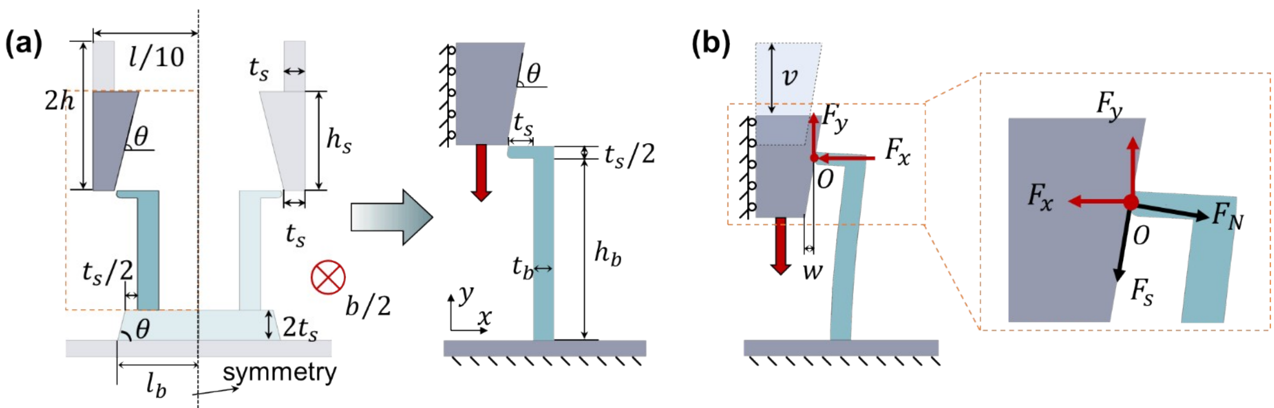

Figure S1. a) Design parameters of the snap-fit structure and its boundary conditions, theoretically analyzed by taking half based on symmetry. b) Deformation state of the snap-fit structure in compression and its force analysis.

The deformation mode of the simplified structure under vertical load is shown in Figure S1b, then the approximate differential equation for the deflection curve of the vertical beam can be written as:

$$EIw^{''} = M(y)\#(S1)$$

where $M(y)$ is the bending moment of the vertical beam, E is material Young's modulus, $I = (bt_b^{3})/12$

is the moment of inertia of the cross section, and w is the deflection of the vertical beam. At the intersection point O between the sliding groove and the vertical beam, the sliding groove is subjected to a vertical force F_y and a horizontal force F_x due to the bending deformation of the vertical beam. By solving the differential equation, the relationship between the horizontal displacement at point O and the horizontal force is given by:

$$F_x = \frac{3wEI}{\left(h_b + t_s/4\right)^3} \#(S2)$$

where it is assumed that the intersection point of the sliding groove and the vertical beam is located at the midpoint of the cantilever hook. For simplicity in the calculation, the length of the vertical beam is approximated as $h_b + t_s/4$.

By projecting the force exerted on the sliding groove onto the normal of the inclined surface, the normal force F_N and the frictional force F_s acting on the vertical beam can be expressed as:

$$F_N = F_x \cdot \sin\theta + F_y \cdot \cos\theta \#(S3)$$

$$F_s = uF_N \#(S4)$$

In which, u is the friction coefficient. By resolving the force applied to the sliding groove onto the inclined surface, the frictional force acting on the vertical beam can be expressed as:

$$F_s = F_y \cdot \sin\theta - F_x \cdot \cos\theta \#(S5)$$

By combining Equations (S4) and (S5), the vertical force F_y on the sliding groove can be determined as:

$$F_y = F_x \cdot \left(\frac{\cos\theta + u\sin\theta}{\sin\theta - \mathrm{u}\cos\theta}\right) \#(S6)$$

Since the vertical displacement v of the sliding groove is related to the horizontal displacement w of the vertical beam by the following equation:

$w = v \cdot \tan^{-1} \theta \#(S7)$

By combining Equations (S2), (S6), and (S7), the vertical force F_y on the vertical beam can be written as:

$$F_y = \frac{vEbt_b^{\ 3}}{4(h_b + t_s/4)^3} \left(\frac{\cos\theta + u\sin\theta}{\sin\theta - \mathrm{u}\cos\theta} \right) \cdot \frac{\cos\theta}{\sin\theta} \#(S8)$$

Therefore, the stiffness K_e of the snap-fit structure during the loading process can be expressed as:

$$K_e = 2 * \frac{Ebt_b^{\ 3}}{4(h_b + t_s/4)^3} \left(\frac{\cos\theta + u\sin\theta}{\sin\theta - \mathrm{u}\cos\theta} \right) \cdot \frac{\cos\theta}{\sin\theta} \#(S9)$$

S2: Theoretical model validation of snap-fit structures

According to the theoretical model, the geometric factors that primarily influence the stiffness of the snap-fit structure are: the height h_b, thickness t_b of the vertical beam, and the inclination angle θ of the sliding groove. Therefore, these key parameters are analyzed individually (the initial geometric parameters are: h_b = 15 mm, t_b = 2 mm, l_b = 15.3 mm, h_s = 13.3 mm, and θ = 80°). To verify the accuracy of the theoretical solution for the snap-fit structure, Figure S2 presents a comparison between the theoretical and FEM results for the snap-fit structure under different key parameters. In the discussion of the vertical beam thickness (Figure S2a), the theoretical solution is generally slightly larger than the simulation result, with a maximum difference of 2.21% (t_b = 1.8 mm). However, in the analysis of the vertical beam height and the inclination angle of the slider (Figures S2b and S2c), this trend is not consistent, with a maximum difference of 2.38% (when h_b = 13.5 mm) and 3.20% (when θ = 79°), respectively. The errors may have arisen due to the small deformation assumption made in the theoretical analysis, which overlooks some of the smaller geometric nonlinear effects. The discrepancies may be attributed to the small deformation assumption made in the theoretical analysis, which neglects minor geometric nonlinear effects. Despite these differences, the overall agreement between the simulation results and the theoretical solutions is satisfactory, indicating that the model and computational methods employed are effective and capable of reliably predicting the stiffness of the snap-fit structure.

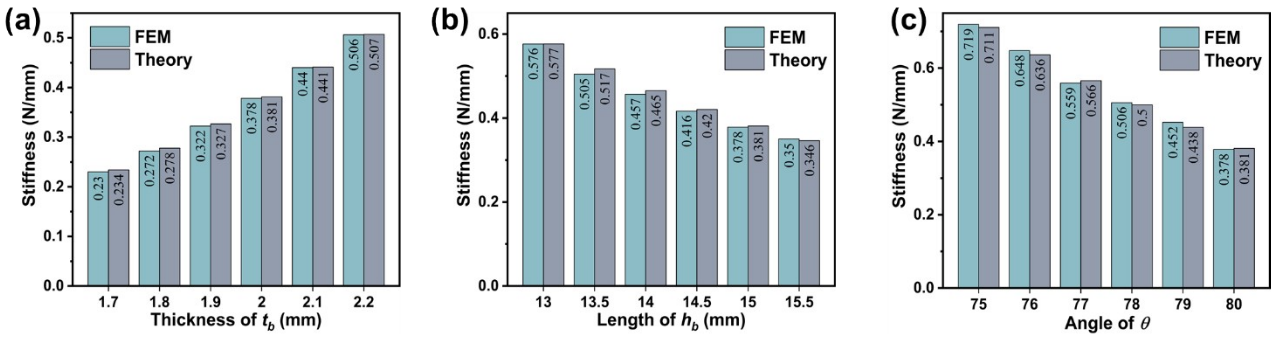

Figure S2. Comparison of theoretical and FEM results for the stiffness of the snap structure for different parameters. a) Thickness of the vertical beam. b) Height of the vertical beam. c) Inclination angle of the sliding groove.

S3: Customized design of curved beams using the KG-MFSE algorithm

The non-gradient KG-MFSE algorithm is used for topology optimization of curved beams with geometrically nonlinear effects to achieve customized design [1]. Here, a material-field series expansion strategy is employed to represent and reduce the dimensionality of the design domain, which is meshed into N elements. Specifically, the projection of the curved beam in the horizontal plane is taken as the design domain, and its material-field function $\chi(r) \in [-1,1]$ is described by the positions r of the observation points (N_p) uniformly distributed within the design domain. $\chi(r)$ can be considered an uncertain bounded field with spatial correlation, where each possible material field function represents a different topological layout. The material distribution at position r is determined by the following condition:

$$\begin{cases} if & -1 \le \chi(r) \le 0, \ \ volid\ material \\ if & 0 < \chi(r) \le 1, \ \ solid\ material \end{cases} \#(S10)$$

The concept of relative density is employed to represent the structural topology in discretized finite element mesh. The relative density ρ_e of element $e = 1, 2, ..., N$ can be expressed as:

$$\rho_e = \rho_{min} + \frac{(1 + \chi(r_e))}{2}(1 + \rho_{min})\#(S11)$$

where r_e is the centroid position of element e, and the minimum value of ρ_e is defined as $\rho_{min} = 0.001$ to avoid numerical issues during the finite element analysis process.

To maintain the connectivity of the material-field function $\chi(r)$, a correlation function C is introduced to describe the spatial correlation of the material-field between any two arbitrary observation points in space:

$$C(r_i,r_j) = e^{-\|r_i - r_j\|^2/l_c^2}\ (i\ and\ j = 1, 2, ..., N_p)\#(S12)$$

in which, l_c is the defined correlation length. The correlation length is set to 30% of the smallest edge length of the structural design domain, which is sufficient to meet the requirements of most optimization designs. Furthermore, for N_p observation points uniformly distributed at the element centroids, the correlation function matrix $C(r)$ of the material field can be expressed as:

$$C(r) = \begin{bmatrix} C(r_1,r_1) & C(r_1,r_2) & \cdots & C(r_1,r_{N_p}) \\ C(r_2,r_1) & C(r_2,r_2) & \cdots & C(r_2,r_{N_p}) \\ \vdots & \vdots & \ddots & \vdots \\ C(r_{N_p},r_1) & C(r_{N_p},r_2) & \cdots & C(r_{N_p},r_{N_p}) \end{bmatrix}\#(S13)$$

To avoid computational difficulties caused by an excessive number of observation points, the first M eigenvectors of the correlation function matrix $C(r)$ are extracted to reduce the dimensionality of the material-field function representation:

$$\chi(r, x) \approx x^T\Lambda^{-1/2}\Phi^T C_d(r)\#(S14)$$

where Λ and Φ are the diagonal matrix of the first M eigenvalues and the matrix of the eigenvectors of the correlation matrix $C(r)$, respectively. Additionally, $C_d(r) = \left\{C(r,r_1),C(r,r_2),...,C\left(r,r_{N_P}\right)\right\}^T$ represents the vector of the correlation functions, and $x = \{x_1, x_2,...,x_M\}^T$ is the reduced vector, with M = 100 as the truncation coefficient.

The values of the material-field function at the observation points need to be constrained within the range shown in Equation (S10). Therefore, the corresponding constraint condition is imposed as follows:

$$x^T W_i x \leq 1, \ \ (i = 1, 2, ..., N_P)\#(S15)$$

where $W_i = \Lambda^{-1/2}\Phi^T C_d(r_i)C_d(r_i)^T \Phi\Lambda^{-1/2}$.

S4: Objective function for topology optimization of curved beams

To define the range of customized stiffness, the negative stiffness region $[v/4, 3v/4]$ (n data points) on the curve is selected. By accurately calculating the slope changes between consecutive data points within this region, the representative negative stiffness values K_i $(i = 1,2,...,n-1)$ are obtained, as shown in Figure 2c. Thus, the objective becomes minimizing the error between the actual negative stiffness of the curved beam K_i and the desired negative stiffness K_e. Additionally, to achieve the expected maximum peak force F_e of the curved beam, the error between the actual maximum peak force F_{max} and F_e should also be minimized. The minimum peak force F_{min} of the curved beam during the loading process is constrained to be less than 0, ensuring that the curved beam maintains its bistable characteristics. To avoid generating results that cannot be applied in engineering, the maximum strain ε_{max} generated during loading is also constrained. Based on this, the topology optimization formulation for the curved beam can be expressed as:

$$\min_{x} \quad R = \left(\frac{1}{n-1} \sum_{i=1}^{n-1} \left((K_i - K_e)/K_e \right)^p \right) + \left((F_{max} - F_e)/F_e \right)^p$$

$$s.t. \quad g_1 = F_{min} - F_s \leq 0 \quad (F_s < 0) \#(S16)$$

$$g_2 = \varepsilon_{max} - \bar{\varepsilon} \leq 0$$

where R represents the sum error of the negative stiffness and the peak force. To ensure these errors are comparable in magnitude, each is normalized accordingly. The parameter p is the penalty factor, selected as an even number to approximate the expected values. In the constraint g_1, the introduction of F_s is intended to ensure that the curved beam retains a distinct bistable characteristic. The parameter $\bar{\varepsilon}$ represents the maximum allowable strain for the material used in fabrication, while the topology layout of the material is denoted by x.

Figure S3 presents the optimization results for the target regions of $[v/3, 2v/3]$, $[v/4, 3v/4]$, and $[v/5, 4v/5]$, with the design objectives uniformly set to K_e = -7.5 N/m and F_e = 7.5 N. It can be observed that when the region is $[v/3, 2v/3]$, the peak force of the force-displacement curve matches the expected value. However, the negative stiffness values are only accurately captured near the central region, with discrepancies increasing toward the sides. When the target regions are $[v/4, 3v/4]$ and $[v/5, 4v/5]$, the negative stiffness values exhibit minor and more consistent deviations from the expected values. Additionally, the extent of the negative stiffness region should not be overly large. During the optimization process, the mechanical characteristics of the curved beam are evaluated within these regions. A larger negative stiffness region results in increased computational time costs for the optimization.

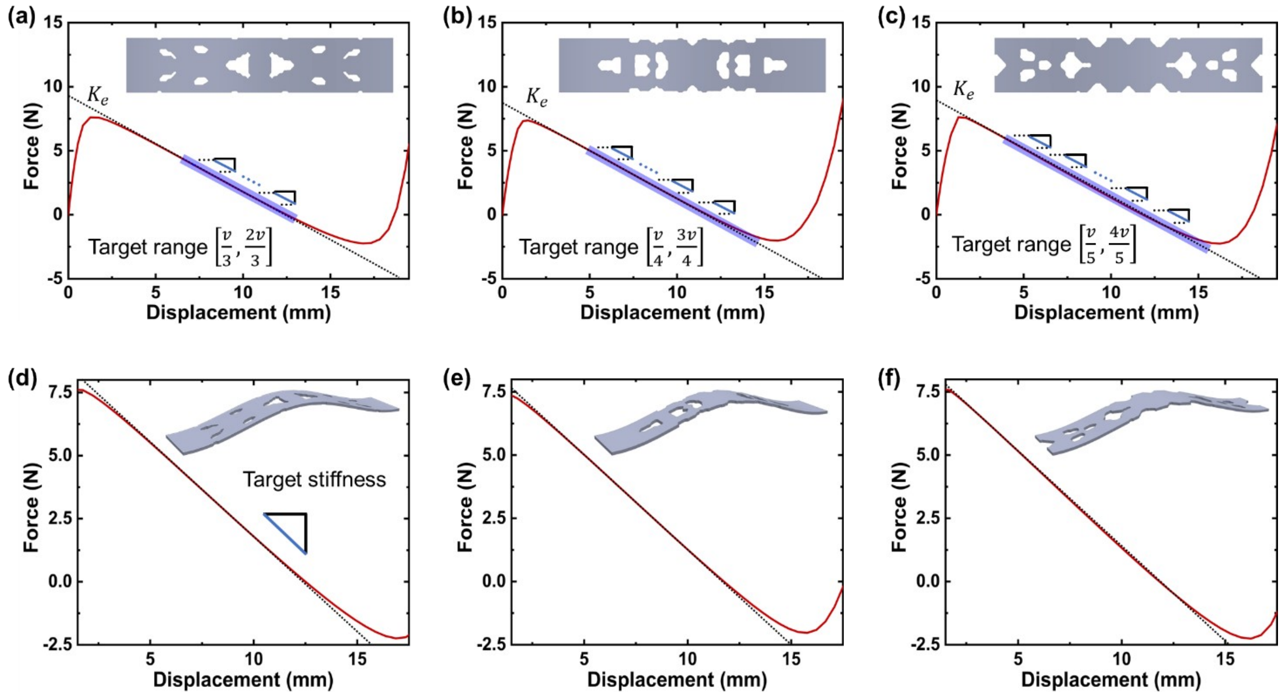

Figure S3. Optimization results for target ranges of a) $[v/3, 2v/3]$, b) $[v/4, 3v/4]$ and c) $[v/5, 4v/5]$, respectively. d-f) Zoomed-in results for the negative stiffness region in Figures (a-c), respectively.

S5: Comparison of responses before and after unit cell assembly

The initial model of the curved beam is illustrated in Figure S4a. Considering the symmetrical geometry and deformation behavior of the curved beam, component blocks were incorporated at both the extremities and the center. This modification allows for the application of boundary conditions and ensures compatibility for the subsequent assembly of unit cells. Figure S4b shows the optimized curved beam, and the resulting bistable unit cell constructed from it is illustrated in Figure S4c. It can be observed that the force-displacement curves of the two models are nearly identical, indicating that the addition of functional components does not compromise the mechanical performance of the curved beam. The final addition of the snap-fit structure constitutes an ideal energy-absorbing unit cell with bistable properties (Figure S4d), achieving the proposed force-displacement curve.

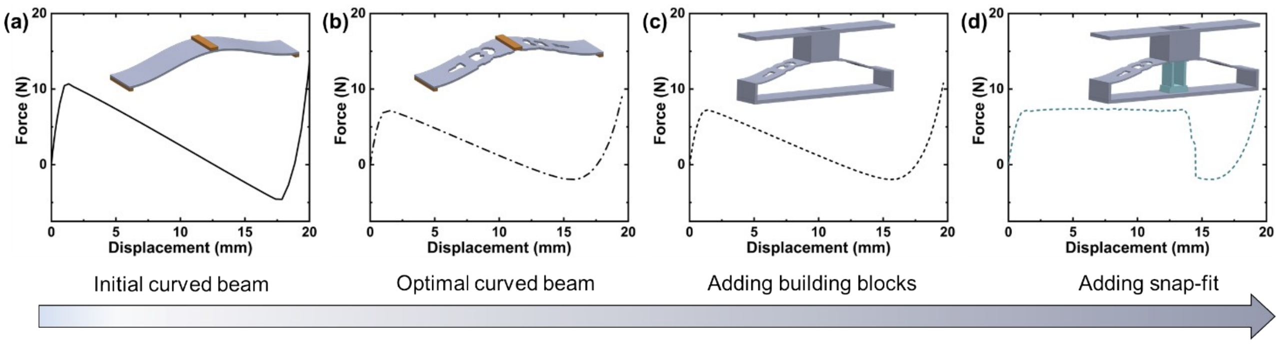

Figure S4. Force-displacement curves obtained from FEM for curved beams in different states. a) Force-displacement curves in the initial state. b) Force-displacement curves after customization by topology optimization. c) Force-displacement curves after equivalent separation of the curved beam and addition of functional parts. d) Force-displacement curve after adding snap-fit structure to assemble into an ideal energy-absorbing unit cell.

S6: Geometric parameters and material Characterization of energy-absorbing unit cells

As mentioned in Section 2.2 of the main text, the geometrical parameters of the unit cell can be adjusted according to requirements. Here, to verify the effectiveness of the design strategy, two sample unit cells are fabricated as needed with the geometric parameters and expected peak forces detailed in Table S1.

Table S1 Geometric parameters of the energy-absorbing unit cells.

Sample	h (mm)	l (mm)	b (mm)	t (mm)	h_b (mm)	h_s (mm)	l_b (mm)	t_s (mm)	t_b (mm)	θ (°)	F_e (N)
1	2	0.2	4.17	1	15	13.3	15.3	2	2	80	7.5
2									2.2		10

To obtain the material model of nylon (polyamide), three dog-bone-shaped samples with dimensions conforming to the ASTM D638 type IV standard are 3D printed, as shown in Figure S5a. Quasi-static tensile tests are then performed using an INSTRON 34TM-10 testing machine at a tensile rate of 1 mm min^{-1}. The nominal stress-strain curves for the three tests are plotted in Figure S5b. By calculating the stress-strain curves for the proportional phase of the material, Young's modulus is taken as E = 807 MPa and Poisson's ratio is taken as υ = 0.3.

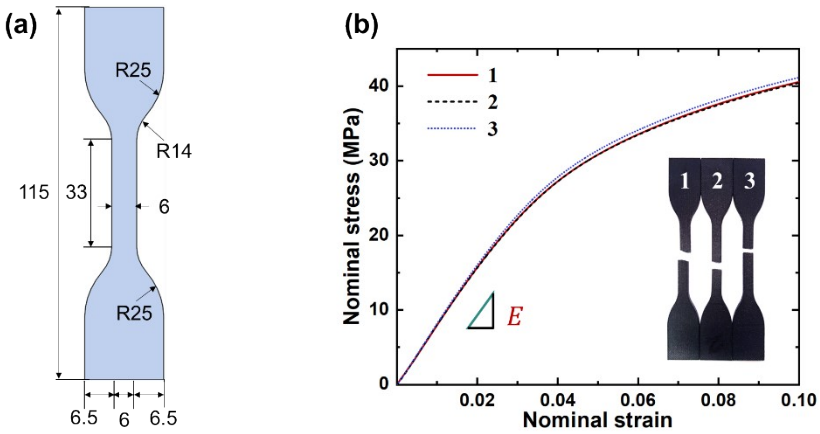

Figure S5. a) The dimensions of the test samples are as per the ASTM D638 type IV standard. b) Nominal stress-strain response of nylon material obtained from three tensile experiments.

The coefficient of friction between nylon surfaces is tested using a high-frequency, high-precision micro-motion friction tester (FFT-M1, Rtec, USA) with a test frequency of 100 Hz and a duration of 60 seconds. The test results are shown in Figure S6, and it can be observed that the nylon material has good abrasion resistance and a stable coefficient of friction. Therefore, the average stable value of the friction coefficient $u = 0.29$ is selected for the finite element simulation.

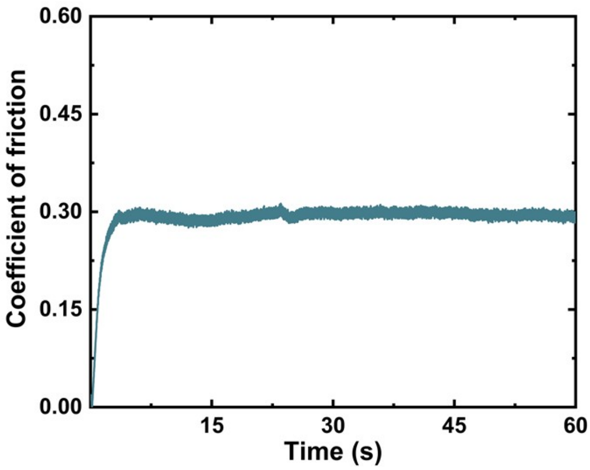

Figure S6. The coefficient of friction test results for nylon.

S7: Customized results for different objectives of curved beams

To evaluate the adaptability of the customized curved beam design, optimizations were performed using different objectives. Figure S7 illustrates the topologically optimized configurations of curved beams with varying combinations of peak force and negative stiffness. Observations indicate that when maintaining the same negative stiffness while reducing the expected peak force, the topology of the curved beam becomes more intricate and utilizes less material. This is because a smaller target peak force reduces the required strength of the curved beam, expanding the design space for material distribution. Consequently, the algorithm can optimize the material layout extensively, resulting in more complex topological configurations. It is important to note that as the expected peak force increases while the negative stiffness decreases, the deviation in the force-displacement curve diminishes. This indicates that when setting the objective function, the target values for peak force and stiffness should be adjusted concurrently to achieve optimal customized designs.

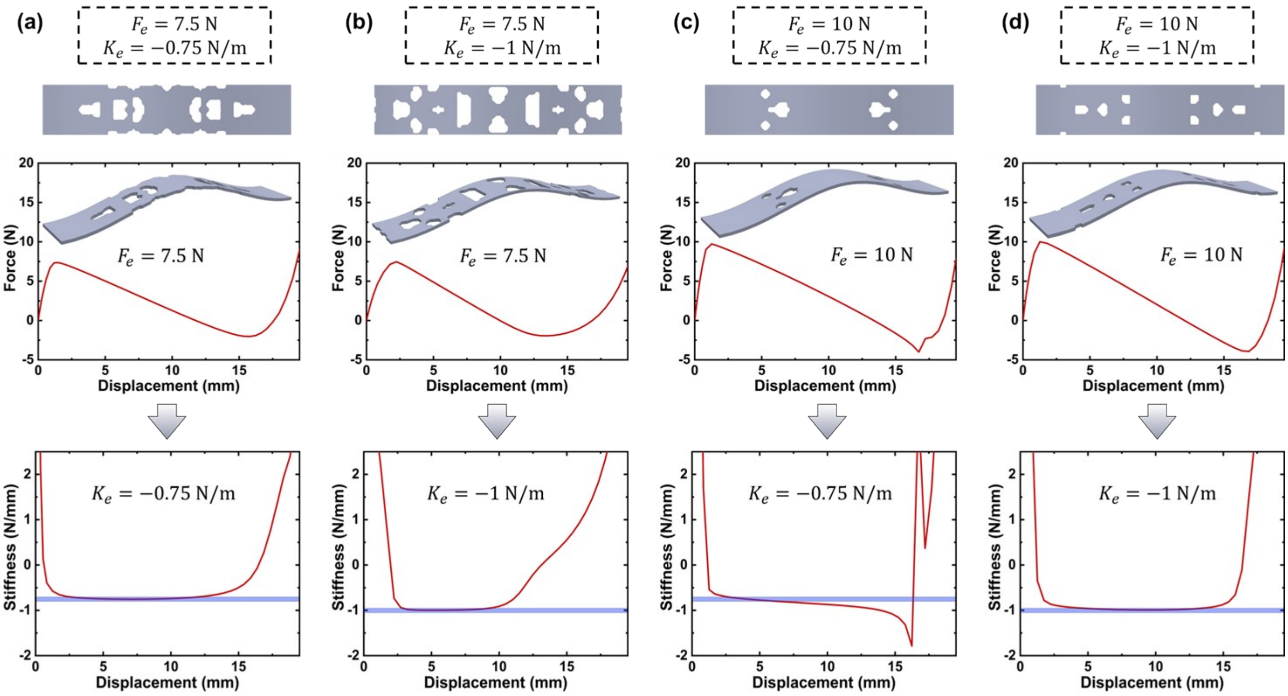

Figure S7. Topological configurations, force-displacement curves, and stiffness curves (derived from the force-displacement curves) of curved beams for different optimization objectives. a) $F_e = 7.5\ N$ and $K_e = -0.75\ N/m$. b) $F_e = 7.5\ N$ and $K_e = -1\ N/m$. c) $F_e = 10\ N$ and $K_e = -0.75\ N/m$. d) $F_e = 10\ N$ and $K_e = -1\ N/m$.

S8: Deformation process of the ideal energy-absorbing unit cell

As shown in Figure S8, quasi-static loading tests were conducted to analyze the mechanical behavior of the Sample-1 unit cell, and the finite element simulations were broadly consistent with the experimental results. During the loading process, the customized curved beam deforms first, providing the initial energy barrier. When the force-displacement curve of the unit cell approaches the negative stiffness region, the snap-fit structure engages, generating a forward force through friction. This results in an ideal rectangular curve and locks the system state upon energy absorption completion. Furthermore, we compared the strains of the curved beam and the snap-fit structure. The results demonstrate that both components play a role in load-bearing, with the maximum strain occurring consistently at the base of the snap-fit structure and the midpoint of the curved beam throughout the deformation process. For example, when the displacement increases from 0 to 14 mm, the strain correspondingly rises from 0 to 0.0397. Nevertheless, this maximum strain remains below the yield strain of the unit cell material. As the unit cell passes the critical point and enters the locked state (from 14 mm to 20 mm), the maximum strain decreases to 0.0261.

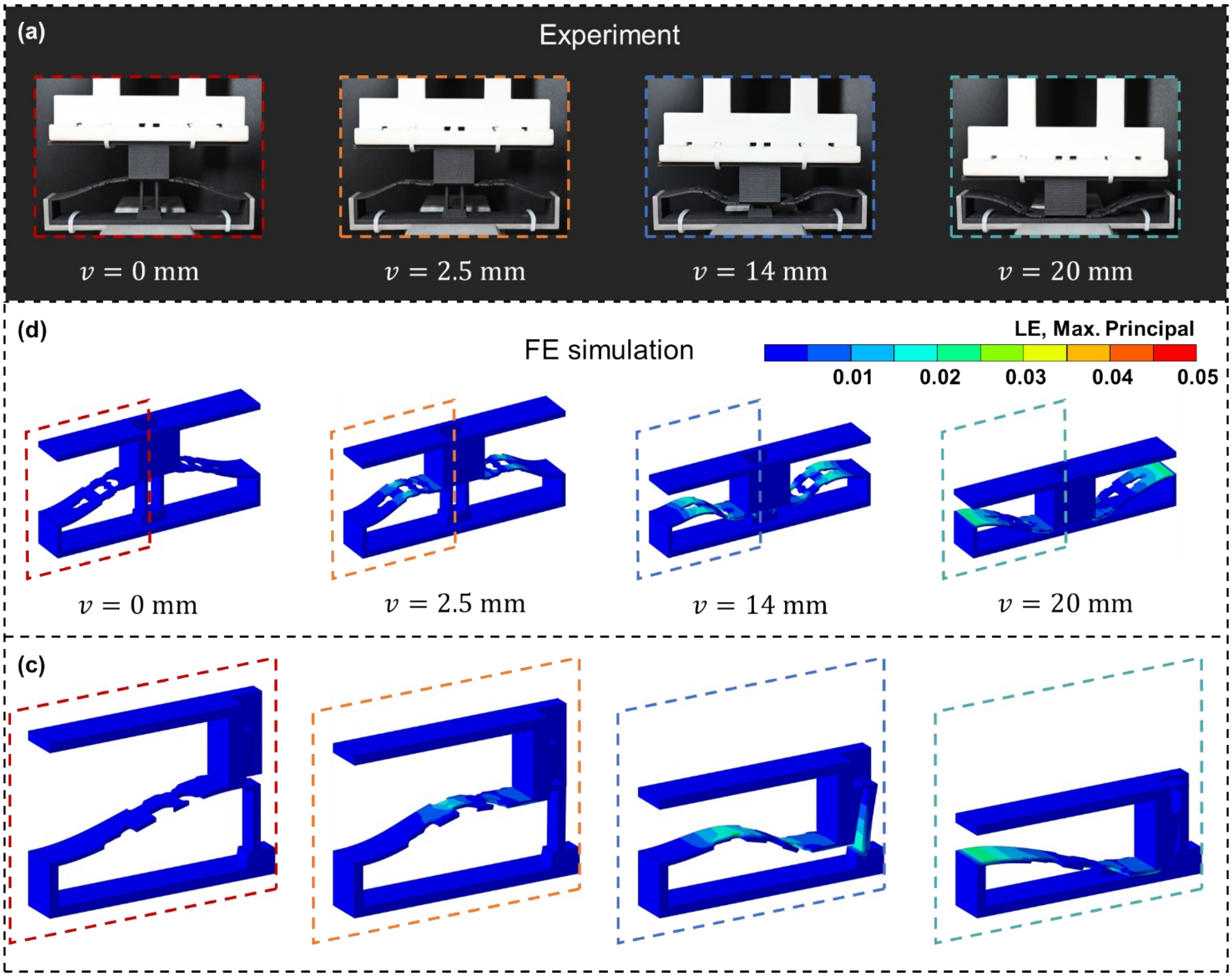

Figure S8. Deformation process of the ideal energy-absorbing unit cell. Comparison of a) experiment and b) finite element simulation results during deformation. c) Stress distribution of the unit cell.

S9: Cyclic loading test for the unit cell

To evaluate the reusability of the metamaterial, we conducted cyclic loading tests on the unit cell. As energy-absorbing metamaterials often exhibit performance degradation after repeated use, cyclic loading tests are a necessary method for assessing the durability and effectiveness of reusable structures. Specifically, we performed 16 loading-unloading cycles on the Sample-1 unit cell under conditions consistent with the quasi-static compression tests. As shown in Figure S9, it can be observed that the unit cell exhibited no damage after multiple cycles, and the force plateau of the first loading and the last loading maintained a small change rate of 7.61% ($\bar{F}$ is defined as the average reaction force over the displacement range of 4-11 mm). This indicates that no significant degradation of the force plateau region has occurred, demonstrating the stable mechanical performance and excellent durability of the unit cell.

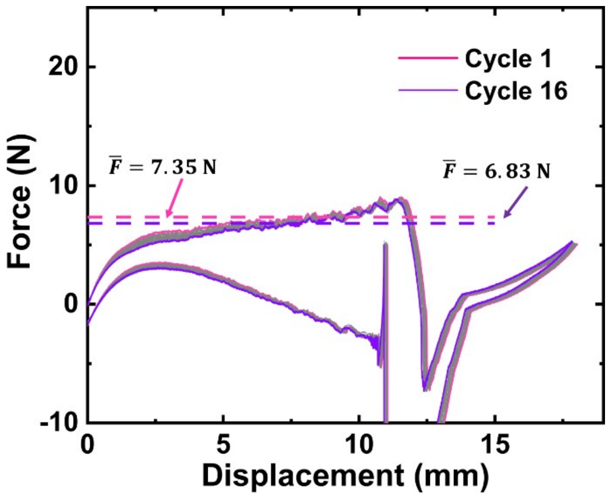

Figure S9. Force-displacement curves of the designed Sample-1 unit cell in cyclic compression tensile tests, where $\bar{F}$ is defined as the average reaction force over the displacement range of 4-11 mm.

S10: Mechanical behavior of the unit cell under different loading rates

To evaluate the impact of the dynamic properties of material parameters on the designed metamaterial, we conducted quasi-static compression experiments on a unit cell at varying loading rates. Specifically, five different loading rates were applied—2.5 mm/min, 5 mm/min, 10 mm/min, 20 mm/min, and 40 mm/min—and the corresponding force-displacement curves are presented in Figure S10. The results indicate that the force plateau of the structure slightly increases with higher loading rates (the difference between the fastest and slowest is about 5.67%), where $\bar{F}$ is defined as the average reaction force over the displacement range of 4-11 mm. This phenomenon may be attributed to the viscoelastic behavior of the material. It is noteworthy that the structure consistently exhibits rectangular force-displacement curves at all loading rates, showing that the mechanical behavior of the metamaterial is mainly governed by its structural design rather than material parameters. This aligns with the design objective of metamaterials, which aims to achieve tailored mechanical responses through microstructural design.

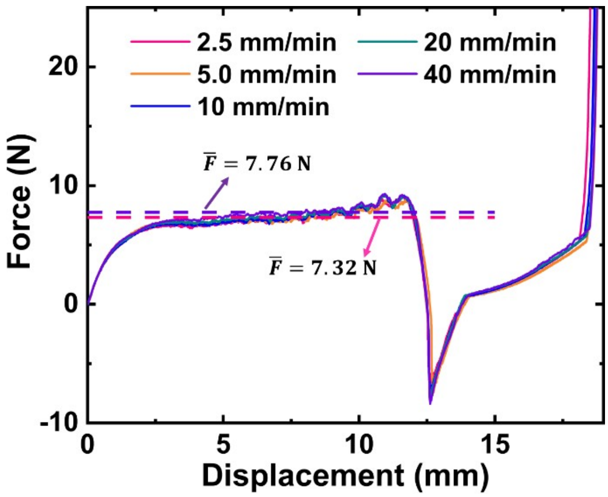

Figure S10. Force-displacement curves of the unit cell at different loading rates, where $\overline{F}$ is defined as the average reaction force over the displacement range of 4-11 mm.

S11: Drop weight impact test with different testing height

Figure S11 presents the results of impact tests in which four types of metamaterials were dropped from a height of 80 mm. A weight with a mass of 1460 g generated an impact energy of 1168 mJ during the drop. Due to the high impact energy, the maximum acceleration occurred after the metamaterial had fully collapsed and decreased as the energy-absorbing capacity increased. Among the tested types, Type II metamaterials, which exhibited the highest energy absorption, demonstrated the best performance with a maximum acceleration of 42.25 m/s². In contrast, Type IV metamaterials, with lower energy absorption capabilities, showed the highest maximum acceleration of 105.38 m/s². Additionally, although the first two peak values of the metamaterials increased compared to low-speed impacts, their magnitudes remained near $A_{collapse} = F_e/M$. This indicates that regulating the force plateau and peak force is still valid for the first acceleration peak.

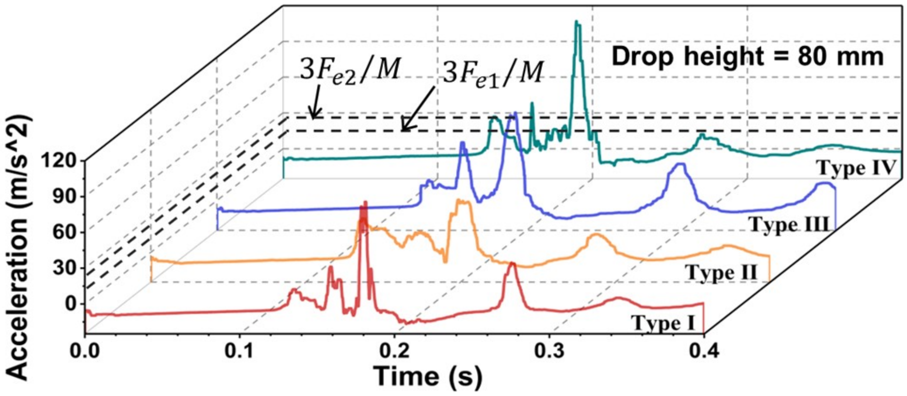

Figure S11. Time-acceleration curves for four types of energy-absorbing metamaterials at an impact height of 80 mm. The horizontal dashed line indicates the force platform of the metamaterial divided by the mass of the weight.

S12: Collision experiment setup of a miniature trailer

The sandbox collision experimental setup for the miniature trailer consists of four main components: a miniature trailer, a protection device made from metamaterials, an impact rod, and an immovable sandbox, as shown in Figure S12a. The sandbox is enclosed by four transparent acrylic panels, with the front panel, back panel, and load-bearing columns 3D printed from resin. These are assembled and filled with uniformly granular colored sand. To minimize the effect of impact velocity on the distance the impact rod travels, the end of the rod inserted into the sandbox is tapered, while the opposite end features a circular impact surface. Additionally, an anti-impact device comprising six unit cells is positioned directly in front of the impact rod for protection. The trailer is positioned a set distance (640 mm) from the protection device to ensure it accelerates to the target speed. During the test, the trailer strikes the protection device, absorbing energy through the metamaterials. The unabsorbed energy is transferred to the impact rod, causing it to penetrate the sandbox. The protective performance of the metamaterials is evaluated by measuring the distance of insertion of the impact rod into the sandbox. And the smaller the insertion distance, the better the protection performance.

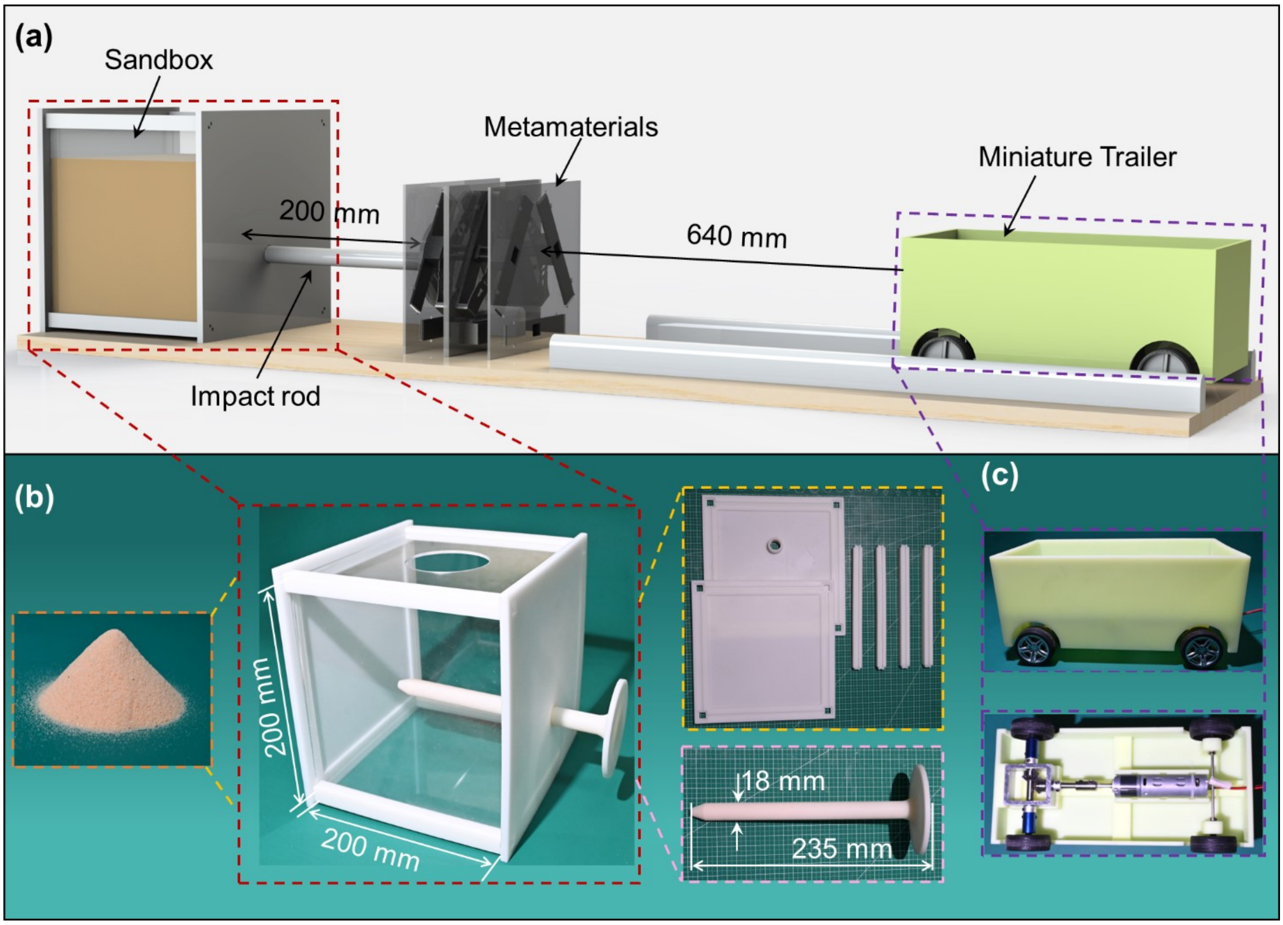

Figure S12. The sandbox collision experimental setup for the miniature trailer. a) Overview of the experimental setup. The experiment setup comprises a miniature trailer, a protection device made from metamaterials, an impact rod, and an immovable sandbox. b) The color sand and sandbox with an impact rod. c) A detailed view of the top and bottom of the miniature trailer is available.

S13: Low-speed collision experiments for miniature trailer

Figure S13 illustrates the impact test of a miniature trailer at a speed of 1.5 m/s, impacting metamaterials of types I-IV with energy-absorbing properties. The Type I metamaterial underwent complete deformation during the test, while the other types deformed only in the first layer. The reason for this phenomenon is that the reduction in impact strength reduces the energy of the car when it hits the metamaterial, and once the metamaterial has completed the deformation of one layer, the energy remaining in the trailer does not reach the deformation barrier of the other layer, preventing the metamaterial from performing full energy absorption. Similar to the results in Figure 5, the designed metamaterials demonstrated improved impact resistance, with Type I showing the best performance. Specifically, after impact, Type I reduced the travel distance of the crash rod to 34 mm, 27.4% of the distance seen with the dense structure. In contrast, the Type II and Type III metamaterials, which experienced partial deformation, allowed the rod to move further, traveling 66 mm and 77 mm, respectively. However, both still performed better than Type IV, which allowed the rod to travel 101 mm. These results show that different force platforms are required for different impact velocities, especially at low impact intensities of 1.5 m/s where type I metamaterials show the best energy absorption capacity due to the smaller threshold.

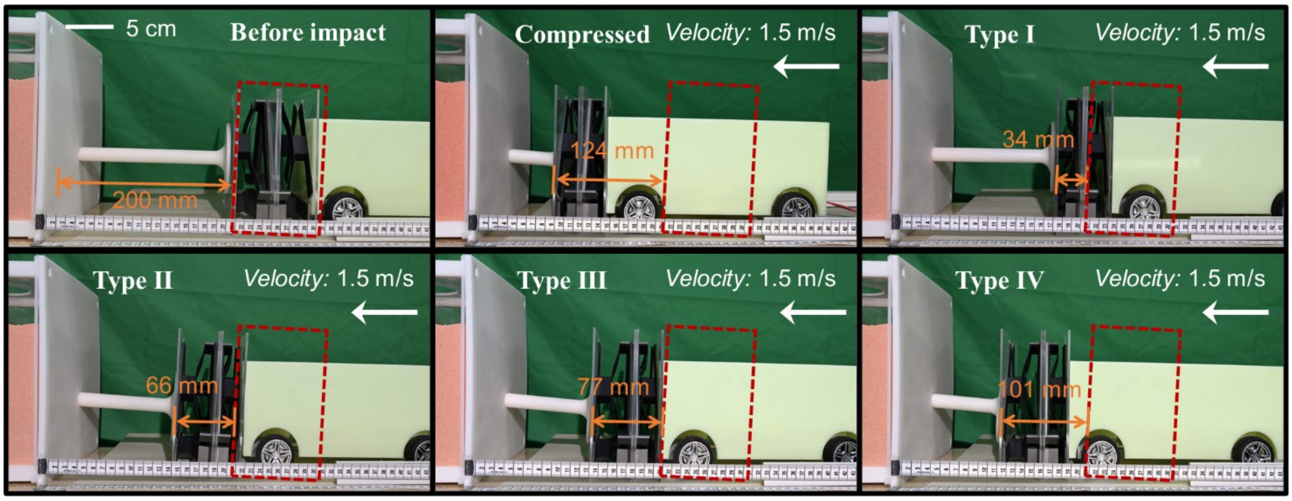

Figure S13. Test results of the miniature trailer impacting metamaterials at a speed of 1.5 m/s.

S14: Force-time dynamic collision experiments for miniature trailers

The experimental setup for the force-time dynamic collision of a miniature trailer consists of four main parts: a miniature trailer, a metamaterial, a barrier, and an acceleration sensor, as shown in Figure

S14(a). During the experiment, a trailer with a mass of 1.86 kg impacted the metamaterial at a speed of 1.5 m/s, and the dynamic response of the trailer was recorded in real time by the sensor. The metamaterial absorbs the kinetic energy of the trailer through deformation, and the stronger the absorption capacity, the smaller the peak force of the cart during the collision. Consequently, the protective performance of the energy-absorbing metamaterial can be evaluated by analyzing the force-time curve. Figure S14(b) illustrates the force-displacement curves during the collision. The designed metamaterial exhibits lower peak force compared to the control group (Type IV), which indicates that the proposed structure has a better cushioning capability. This result is consistent with the results observed in the miniature trailer impact experiment shown in Figure 5. Figure S14(c) shows a snapshot of the Type I metamaterial in the impact test, demonstrating the deformation process of the structure during impact.

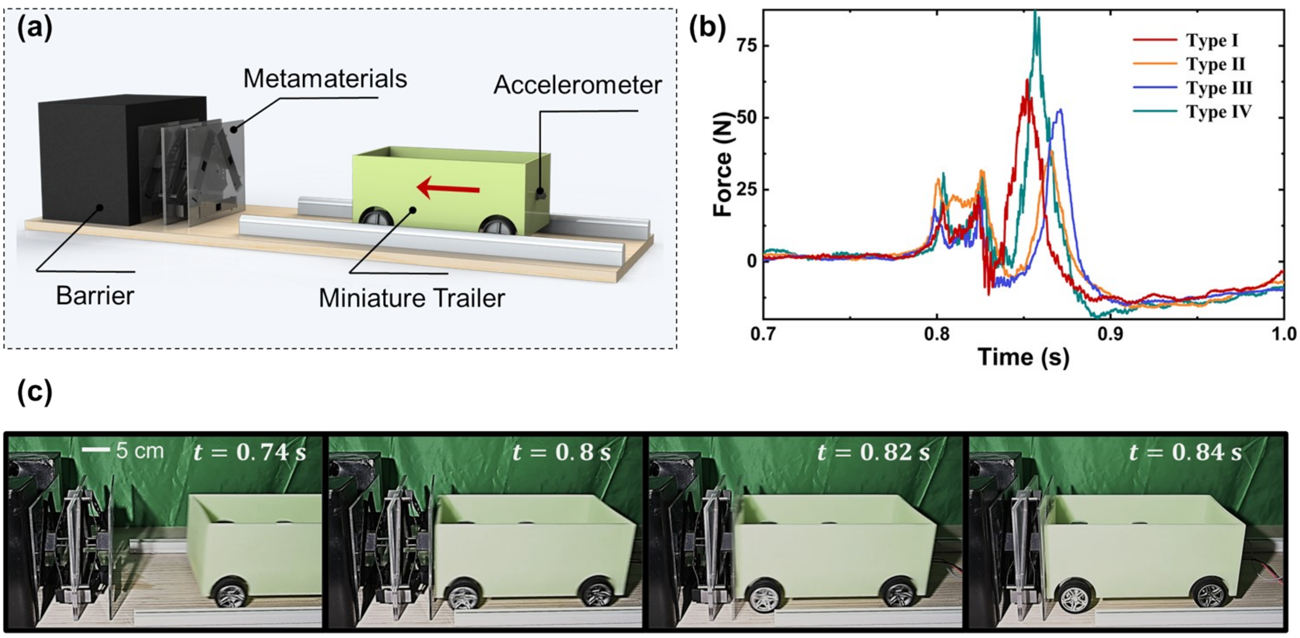

Figure S14. Experimental results of force-time dynamic crash experiments on miniature trailers. a) Overview of the experimental setup. b) The time-force curves of energy-absorbing metamaterials. c) Snapshots of Type I metamaterial during impacts.

S15: 2D and 3D energy-absorbing metamaterials

The designed unit cells can be arranged to form 2D and 3D energy-absorbing metamaterials. For example, the initial and deformed states of the 2D metamaterial are shown in Figure S15a, illustrating its ability to absorb energy in both directions upon impact. Figure S15b demonstrates the designed 3D cell, and the 3D energy-absorbing metamaterial is formed by arraying the cells. The simulation results in Figure S15c show the strain distribution after deformation. It can be noticed that the maximum strain occurs in the curved beam and snap structure, indicating that the combined design does not increase the risk of structural failure during deformation. Experimental measurements also confirm that the observed deformation matches the finite element simulations (Figure S15d). This means that the 2D design efficiently captures energy in the plane, while the 3D design increases the versatility and energy-absorbing capacity of the metamaterials, making them suitable for a broad range of practical applications.

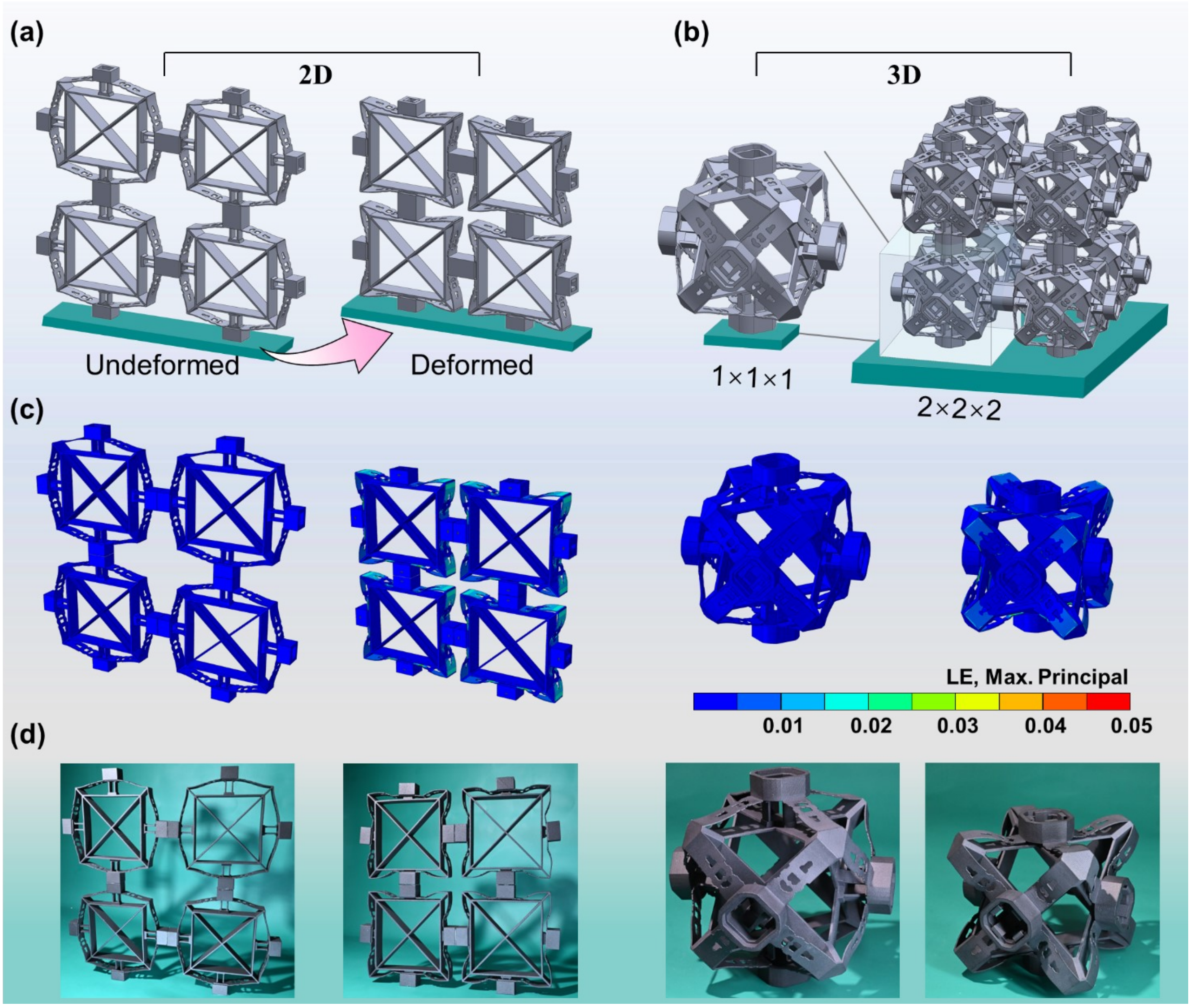

Figure S15. Schematic views of the proposed a) 2D and b) 3D energy-absorbing metamaterials, with their c) strain distribution and d) 3D printed samples.

S16: Finite element simulations of the ideal energy-absorbing unit cell

The commercial finite element simulation software ABAQUS (Simulia) is utilized for finite element simulations, and the material properties of nylon are measured by tensile tests (Young's modulus and Poisson's ratio). A static general solver is used to calculate the mechanical response of the unit cell to obtain smooth force-displacement curves. In this simulation, geometrical nonlinearities are turned on to deal with the large deformations and complex frictional contacts during the calculations. Both normal and tangential behavior of the contact surfaces are considered. The normal contact behavior was modeled as "hard" contact, while the tangential behavior is defined using a penalized friction model with a coefficient of $u = 0.29$. The finite element model is shown in Figure S16a, where an eight-node linear hexahedral element (C3D8R) is used for meshing, and at least four solid meshes are generated along the thickness direction of the curved beam to simulate the bending of the curved beam accurately. Figure S16b shows the calculation results for different meshes, indicating that a mesh size of 0.85 mm is sufficient to obtain accurate finite element simulation results.

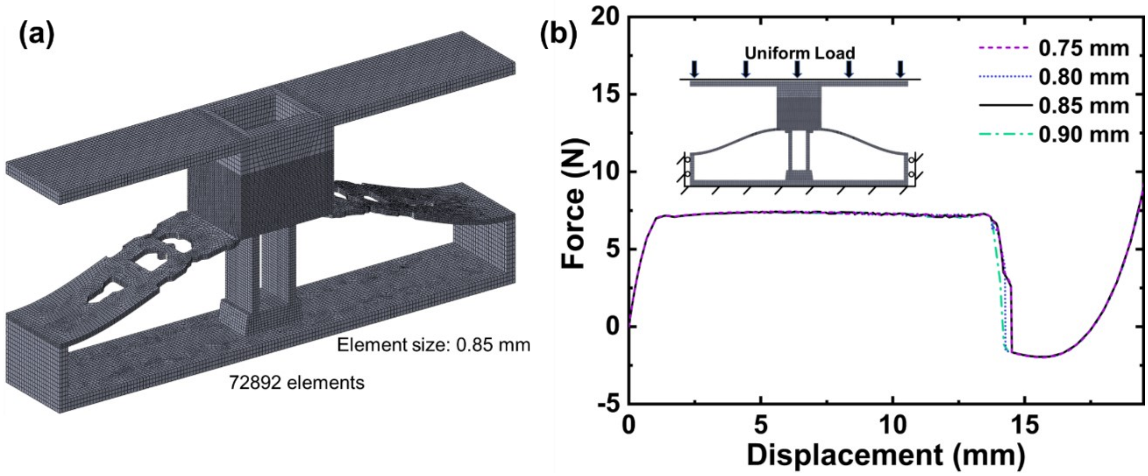

Figure S16. a) Finite element model of the ideal energy-absorbing unit cell (total of 72892 elements). b) Compression conditions of the unit cell and force-displacement curves for different element sizes.

S17: The measured in-plane thickness of the curved beams and snap-fit structures in the 3D-printed metamaterial samples

Measurements were made on prepared samples 1 and 2, and the results are shown in Figure S17. The maximum deviation of the measurements from the design thickness is 6%.

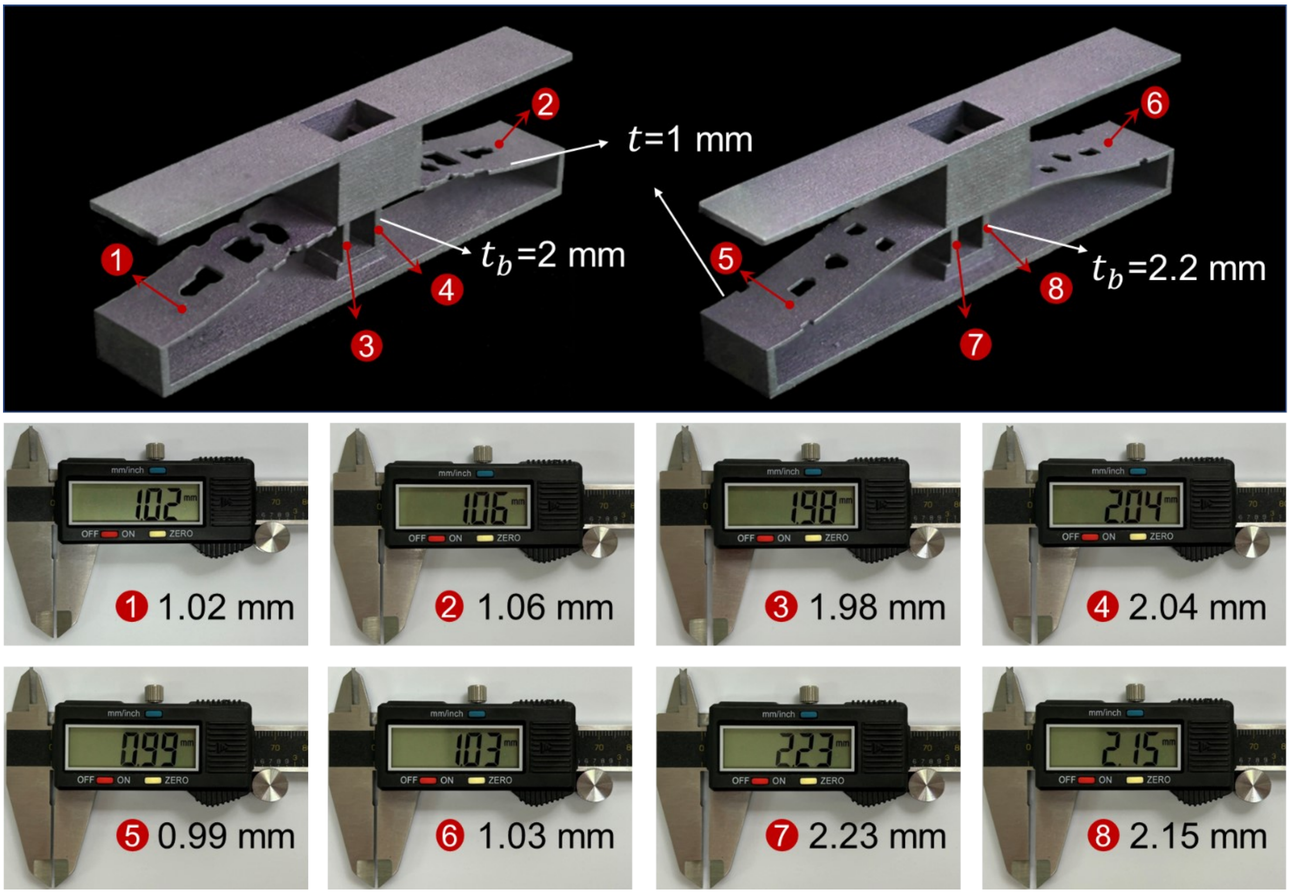

Figure S17. The measured in-plane thickness of the curved beams and snap-fit structures in the 3D-printed unit cells.

References

1. Luo, Y., Xing, J. & Kang, Z. Topology optimization using material-field series expansion and Kriging-based algorithm: An effective non-gradient method. *Comput. Methods Appl. Mech. Eng.* **364**, 112966 (2020).